1   **The story of a summit nucleus:**

2   **Hillslope boulders and their effect on erosional patterns and landscape morphology**

3   **in the Chilean Coastal Cordillera**

4   Emma Lodes[1*], Dirk Scherler[1,2], Renee van Dongen,[3] and Hella Wittmann[1]

5   [1]GFZ German Research Centre for Geosciences, Telegrafenberg, 14473 Potsdam, Germany

6   [2]Freie Universität Berlin, Institute of Geological Sciences, 12249 Berlin, Germany

7   [3]International Centre for Water Resources and Global Change, 56068 Koblenz, Germany

8   *Corresponding author (lodes@gfz-potsdam.de)

10   **Key words:** [10]Be; cosmogenic nuclides; Chilean Coastal Cordillera; fractures; landscape

11   morphology; grain size; hillslope denudation rates

13   **Abstract**

14   While landscapes are broadly sculpted by tectonics and climate, on a catchment scale, the

15   density of bedrock fractures can influence hillslope denudation rates and dictate the location of

16   topographic highs and valleys. In this work, we used [10]Be cosmogenic radionuclide analysis to

17   measure the denudation rates of bedrock, boulders, and soil, in three granitic landscapes with

18   different climates in Chile, with the hypothesis that high fracture density reduces grain size and

19   increases denudation rates. Denudation rates range from 10 to 15 m Myr^{-1} for bedrock and

20   boulders and from 15 to 20 m Myr^{-1} for soil in the humid and semi-arid climates, and are higher

21   in the mediterranean climate (~40-140 m Myr^{-1}), likely due to steeper slopes. We found that

22   hillslope bedrock and boulders erode more slowly than the surrounding soil in the diffusively-

23   eroding study sites. Furthermore, across a bedrock ridge in the humid site, bedrock denudation

24   rates increase with fracture density. These findings are consistent with the observation that

25   streams in our field sites follow the orientation of at least one major fault orientation. Our results

26   suggest that tectonically-induced fractures and faults dictate landscape evolution through

27   reducing grain size and thus enhancing differential denudation rates.

1   Introduction

30   Landscapes on earth are shaped by tectonic uplift and climate, which dictate erosional and

31   weathering regimes over geologic timescales. When uplift and climate are held constant

32   sufficiently long, fluvial landscapes reach a steady state, in which the slopes of hills and stream

33   channels adjust so that denudation rates match tectonic uplift rates (e.g. Burbank et al., 1996;

34   Kirby and Whipple, 2012). Variations in bedrock strength and the grain size of hillslope

35   sediment, however, exert additional control on the morphology of hills and valleys (e.g. Attal et

36   al., 2015; Glade et al., 2017). Initially, hillslope sediment size is set by lithology and the density

37   of fractures, which are formed due to tectonic and topographic stresses (e.g. Molnar et al., 2007;

38   Roy et al., 2016; St. Claire et al., 2015; Sklar et al., 2017). Near the earth surface, water, often

39   carrying biotic acids, infiltrates bedrock fractures and promotes chemical weathering that further

40   reduces sediment size and converts bedrock to regolith (Lebedeva and Brantley, 2017; Hayes et

41   al., 2020). Therefore, long residence times of sediment in the weathering zone, being the

42   consequence of slow erosion, may result in complete disintegration of bedrock and the formation

43   of saprolite and soil, whereas rapid erosion and short residence times can lead to hillslope

44   sediment size limited by fracture spacing (e.g. Sklar et al., 2017; Attal et al., 2015; Roda-Boluda

45   et al., 2018; van Dongen et al.., 2019).

46   Soil-mantled hillslopes are typically considered to be dominated by diffusive processes,

47   for which conceptual models and geomorphic transport laws are relatively well-established (e.g.,

48   Dietrich et al., 2003; Perron, 2011). However, these models generally assume uniform hillslope

49   material and do not account for the exhumation of larger boulders through the critical zone (we

50   refer to large hillslope sediment as boulders, but they could also be considered corestones or tors).

51   Neely et al. (2019) addressed erosion and soil transport on mixed bedrock and soil-covered

52   hillslopes using a nonlinear diffusion model, assuming the same denudation rate for bedrock and

53   soil. Often, however, bedrock and large boulders protrude above the surrounding soil, indicating

54   that they are eroding more slowly than the soil, and that denudation rates of boulders are lower

55   than soil transport rates (Oberlander, 1972; Bierman, 1994; Portenga and Bierman, 2011). Once

56   exposed, larger boulders require greater forces to be moved, which can be achieved by steepening

57   slopes (Granger et al., 2001; DiBiase et al., 2018; Neely and DiBiase, 2020), or by lengthening

58   residence until subaerial weathering has decreased their size sufficiently to be transported

59   downslope. During this prolonged residence time, boulders can shield hillslopes from erosion

60   (Glade et al., 2017), and stream channels from incision (Shobe et al., 2016). In terrain where

61   spatial gradients in bedrock fracture spacing result in spatial gradients of hillslope sediment size,

62   it is thus reasonable to expect that the resistance of surface boulders to weathering and transport

63   ought to retard erosion locally, resulting in spatially differential erosion. Moreover, because

64   smaller blocks are easier to move (Shobe et al., 2016), we would expect that rivers preferentially

65   incise in zones of intensely fractured rocks that align with the orientation of faults (Molnar et al.,

66   2007; Roy et al., 2016).

67   In this study, we examined the roles of fractures and hillslope boulders on landscape

68   evolution by quantifying bedrock, boulder, and soil denudation rates along the granitic Coastal

69   Cordillera of Chile, using *in situ* cosmogenic [10]Be. By developing a simple model to convert [10]Be

70   concentrations from boulders into soil and boulder denudation rates and by examining our field

71   sites for signs of fracture control on landscape morphology, we tested the following hypotheses:

72   a) on a hillslope, boulders affect differential erosion by eroding more slowly than the surrounding

73   soil, and b) more highly fractured bedrock is more susceptible to erosion and stream incision than

74   intact bedrock.

75   **2   Field sites**

76   The Chilean Coastal Cordillera, a series of batholiths in the forearc of the Andean

77   subduction zone, lies along a marked climate gradient with humid conditions in the south and

78   hyper-arid conditions in the north (Fig. 1). The Andean subduction zone, in which the Nazca

79   Plate subducts under the South American Plate, has been active since at least Jurassic times (e.g.,

80   Coira et al., 1982). In this study we investigated three field sites along the Coastal Cordillera from

81   south to north: Nahuelbuta National Park, (NA), with a humid-temperate climate, La Campana

82   National Park (LC), with a mediterranean climate, and Private Reserve Santa Gracia (SG), with a

83   semi-arid climate (Fig. 1). All three sites are underlain by granitoid bedrock (Oeser et al., 2018),

84   none show any signs of former glaciation, and all are located on protected land, away from major

85   human influence, such as mines, dams, and large infrastructure. In all three sites, denudation rates

86   from [10]Be cosmogenic radionuclide analysis have been reported by van Dongen et al. (2019)

87   (catchment average rates), and Schaller et al. (2018) (soil pits).

88   NA is located on an uplifted, fault-bounded block (plateau), an unusually high part of the

89   Coastal Cordillera with a mean elevation of ~1300 m above sea level. All of the measurements in

90   this work are from the plateau (~9° mean slope). Tectonic uplift rates in NA increased from 0.03–

91   0.04 to >0.2 mm year^{-1} at 4±1.2 Ma (Glodny et al., 2008), a shift that is also recorded by

92   knickpoints in streams that drain the plateau. [10]Be-derived denudation rates are around 30 m Myr^{-}

93   [1] (Schaller et al., 2018; van Dongen et al., 2019). The main catchment in LC has a mean elevation

94   of 1323 m with a mean slope of 23°, and regional uplift rates are estimated to be <0.1 mm yr^{-1}

95   (Melnick, 2016). Van Dongen et al. (2019) reported a catchment average denudation rate of ~200

96   m Myr^{-1} for a sub-catchment in LC, and Schaller et al. (2018) reported soil denudation rates of

97   40-55 m Myr^{-1}. In SG, the mean elevation is 773 m above sea level, the mean slope is 17.2°, and

98   uplift rates are <0.1 mm year^{-1} (Melnick, 2016). Previously reported ^{10}Be-derived denudation

99   rates are ~9-16 m Myr^{-1} (Schaller et al., 2018; van Dongen et al., 2019).

100   **3   Methods**

101   **3.1   In situ ^{10}Be analysis**

102   **3.1.1   Sample collection**

103   We collected samples for cosmogenic ^{10}Be analysis from bedrock, boulders, and soil to

104   estimate denudation rates from our field sites, targeting hillslopes near previously-collected

105   catchment average and soil pit samples from van Dongen et al (2019) and Schaller et al. (2020).

106   Bedrock samples were taken from an area of up to ~20 m × 20 m (on ridge tops or hillslopes) and

107   consist of an amalgamation of at least ten chips (~25 cm^2 and <2 cm thick), with which we aim to

108   obtain representative mean values of denudation rates that are potentially variable due to episodic

109   erosion by spalling rock chips (Small et al., 1997). Similarly, for boulder samples, one chip was

110   taken from the top of each of at least ten similarly-sized boulders and amalgamated for an area of

111   up to ~40 m × 40 m, depending on boulder abundance. We targeted boulders that appear to be in

112   situ, based on the observation that they are tightly imbedded in the ground. In places with many

113   various-sized boulders, we collected samples from different protrusion heights (~1-m tall

114   boulders, ~0.5-m tall boulders, etc.). Each sampled boulder was measured along the a, b, and c

115   axes, and the protrusion height was noted (see Table 1). Topsoil samples were also collected by

116   amalgamation in the area surrounding the sampled boulders.

117   In NA, we collected five bedrock samples from an area called "Piedra de Aguila" from

118   outcrops with different fracture densities, and measured fracture spacing by stringing a measuring

119   tape along the bedrock surface and measuring the distance between fractures that were at least 1

120   mm wide (Fig. 2A and 2B). We further collected six boulder samples and three soil samples from

121   the ridge and hillslope of "Cerro Anay" (Fig. 1 and 2C), an area called "Casa de Piedras", and a

122   hillslope near the soil pits that were sampled by Schaller et al. (2018). In LC and SG, we were not

123   able to directly measure fracture density due to rarely exposed bedrock. In LC, we took one

124   bedrock sample, two boulder samples and two soil samples from the ridge and slope of "Cerro

125   Cabra" (Fig. 1 and 2D), and three boulder samples and three soil samples from the ridge, upper

126   slope, and lower slope of "Cerro Guanaco" (Fig. 1 and 2F). In SG, we took four bulder samples

127   and three soil samples from the ridge and slope of a hill we termed "Santa Gracia Hill," which

128   also hosts the soil pits of Schaller et al. (2018) (Fig. 1, 2H, and 2I).

129

130   **3.1.2 Analytical methods**

131   We dried, crushed, and sieved amalgamated bedrock and boulder samples for quartz

132   mineral separation, and dried and sieved soils, each to 250-500 micrometer particle size, or to

133   250-1000 micrometers if the 250-500 micrometer sample amount wasn't sufficient. We used

134   standard physical and chemical separation methods to isolate ~20 g of pure quartz from each

135   sample. After spiking each sample with 150 μg of ^{9}Be carrier and dissolving the quartz in

136   concentrated hydrofluoric acid, we extracted Be following protocols adapted from von

137   Blanckenburg et al. (2004). ^{10}Be/^{9}Be$_{(carrier)}$ ratios were measured by accelerator mass

138   spectrometry at the University of Cologne, Germany (Dewald et al., 2013). Sample ratios were

139   normalized to standards KN01-6-2 and KN01-5-3 with ratios of 5.35×10^{-13} and 6.320×10^{-12},

140   respectively. Final ^{10}Be concentrations were corrected by process blanks with an average

141   Be^{10}/Be^{9} ratio of $(2.21 \pm 0.25) \times 10^{-14}$.

142   **3.1.3   Denudation rate calculations**

143   In order to calculate denudation rates from the measured ^{10}Be concentrations, we

144   evaluated bedrock, boulder, and soil samples differently. Bedrock samples present the simplest

145   case, in which we assumed steady state erosion and calculated bedrock denudation rates (ϵ_{br})

146   using the CRONUS online calculator v2.3 (Balco et al., 2008). The steady state assumption is

147   based on our amalgamated sampling, and follows the results of Small et al. (1997), who showed

148   that an amalgamation of several individual bedrock samples is a reasonable approximation of the

149   long-term average denudation rate in episodically eroding settings.

150   Boulder and soil samples require a more nuanced assessment. Boulders protrude above

151   the ground surface, which implies that the lowering of the ground surface (i.e., the soil

152   denudation rate, ϵ_s) is faster than the lowering of the boulder's surfaces (i.e., the boulder

153   denudation rate, ϵ_b) (Fig. 3). Thus, even while they are buried and covered by soil, boulders are

154   exposed to cosmic rays for a significant amount of time prior to breaching the surface (Fig. 3A).

155   We refer to this time span as phase 1. When boulders breach the surface, they should have a

156   concentration similar to that of the surrounding soil (Fig. 3B). As boulders are exposed during

157   phase 2, nuclide production and decay continues, but it takes time for the boulder surfaces to

158   attain a ^{10}Be concentration that is in equilibrium with the slower boulder denudation rate. Thus,

159   we expect that the measured concentrations from the tops of boulders are combinations of the two

160   different phases in which ^{10}Be is accumulated at different rates. Converting the ^{10}Be

161   concentrations of soil samples collected from around the boulders to a denudation rate also

162 requires a special approach, as these samples include an unknown number of grains eroded off

163 boulders, which ought to increase the [10]Be concentration, due to the slower denudation rate of

164 boulders, as compared to soil.

165   Because of the above complications, we used an approach to estimate the soil and boulder

166 denudation rates that considers the measured boulder protrusion heights and their measured [10]Be

167 concentrations. We first calculated the modelled [10]Be concentrations (N, in atoms g^{-1}) by

168 approximating the production rate profile with a combination of several exponential functions

169 (e.g., Braucher et al., 2011) during the two different phases:

$$N = \sum_i \frac{P_i(0)}{\lambda + \frac{\epsilon_s \rho}{\Lambda_i}} e^{-t_2 \lambda} + \sum_i \frac{P_i(0)}{\lambda + \frac{\epsilon_b \rho}{\Lambda_i}} \left[1 - e^{-t_2 (\lambda + \frac{\epsilon_b \rho}{\Lambda_i})}\right]$$ (1),

170 where i indicates different terms for the production by spallation, fast muons, and negative

171 muons; $P_i(0)$ are the site-specific [10]Be surface production rates in atoms g^{-1} yr^{-1} for the different

172 production pathways (Table 1); λ is the [10]Be decay constant (4.9975×10^{-7}); ϵ_b is the boulder

173 denudation rate (cm yr^{-1}); ρ is the boulder density (here we use a value of 2.6 g cm^{-3} for all

174 samples); and Λ_i is the attenuation length scale (160 g cm^{-2} for spallation, 4320 g cm^{-2} for fast

175 muons, and 1500 g cm^{-2} for negative muons, respectively (Braucher et al., 2011). Surface

176 production rates by spallation are based on a SLHL (sea level high latitude) reference production

177 rate of 4.01 atoms g^{-1} yr^{-1} (Borchers et al., 2016) and the time constant spallation production rate

178 scaling scheme of Lal (1991) and Stone (2000) ('St' in Balco et al., 2008). Surface production

179 rates by muons were obtained using the MATLAB-function 'P_mu_total.m' of Balco et al.

180 (2008). Topographic shielding at each sampling site was calculated with the function

181 'toposhielding.m' of the TopoToolbox v2 (Schwanghart and Scherler, 2014) and 12.5-meter

182 resolution ALOS PALSAR-derived digital elevation models (DEMs) from the Alaska Satellite

183 Facility. In equation 1, the first term represents phase 1 and the second term represents phase 2,

184   with t_2 being the exposure time of the boulder, calculated from the height of the boulder (z)

185   divided by the difference between the soil denudation rate and the boulder denudation rate:

$$t_2 = \frac{z}{(\epsilon_s - \epsilon_b)} \tag{2}$$

186   For each sample and associated average boulder protrusion height, we modelled [10]Be

187   concentrations with equation 1 for different combinations of soil and boulder denudation rates

188   that we allowed to vary between 5 and 50 m Myr[-1] (NA and SG), and between 10 and 300 m Myr[-

189   [1] (LC), guided by previously published denudation rate estimates (Schaller et al., 2018; van

190   Dongen et al., 2019). We consider permissible denudation rates as those for which the difference

191   between the modelled and observed [10]Be concentrations is less than the measured 2σ

192   concentration uncertainty.

193   **3.2   Topographic analysis**

194   To test if stream orientations in our field sites follow fault orientations, we analyzed the

195   orientations of streams using one-meter resolution LiDAR DEMs (Kügler et al., 2022). Within

196   each DEM, we first calculated stream networks based on flow accumulation area thresholds of

197   10^4, 10^5 and 10^6 m^2. The lowest threshold was determined based on the occurrence of incised

198   channels visible in the DEMs. We then used the TopoToolbox function 'orientation' with a

199   default smoothing factor (K) of 100, to obtain the orientation of each node in the stream network.

200   To obtain the orientation of mapped faults, we extracted faults within ~50 km of each sampling

201   site from a 1:1,000,000-scale geological map from Chile's National Geology and Mining Service

202   in ArcGIS (SERNAGEOMIN, 2003). Fault orientations were measured for straight fault

203   segments with a length of 100 m. Because we are only interested in the strike of streams and

204   faults, all orientations lie between 0° and 180°. For displaying purposes in rose diagrams, we

205   mirrored these values around the diagram origin by duplicating values and adding 180°.

4 Results

4.1 ^{10}Be concentrations

Measured ^{10}Be concentrations span a wide range of values, and are generally lowest in LC and higher in NA and SG (Table 1). Within NA, we observe the lowest averaged ^{10}Be concentrations (normalized to SLHL) for soil samples ($\mu \pm 1\sigma = 1.41\times10^5 \pm 0.031\times10^5$ atoms g^{-1}), followed by bedrock samples ($2.19\times10^5 \pm 0.036\times10^5$ atoms g^{-1}) and boulder samples ($2.82\times10^5 \pm 0.041\times10^5$ atoms g^{-1}) (Fig. 4). In NA at Piedra de Aguila, where we were able to measure fracture spacing in areas with exposed bedrock, the ^{10}Be concentrations of samples from fractured bedrock decrease with increasing fracture density (Fig. 4A). One boulder sample from the slope of Soil Pit Hill stands out with a concentration that is lower than most soil samples. Similar average values as in NA are attained in SG, with soil samples ($1.70\times10^5 \pm 0.039\times10^5$ atoms g^{-1}) being lower than boulder samples ($3.23\times10^5 \pm 0.059\times10^5$ atoms g^{-1}) (Fig. 4C). Only in LC are the averaged differences between soil ($0.82\times10^5 \pm 0.022\times10^5$ atoms g^{-1}) and boulder samples ($0.74\times10^5 \pm 0.025\times10^5$ atoms g^{-1}) small (Fig. 4B). In addition, at 3 out of 5 sampling locations in LC, boulders have lower concentrations than adjacent soil samples, inconsistent with the assumption that $\epsilon_s < \epsilon_b$ (see section 3.1.3). However, our single bedrock sample from LC has a higher concentration of $1.38\times10^5 \pm 0.082\times10^5$ atoms g^{-1}. Finally, in all three field sites, boulder samples from slope locations have usually lower ^{10}Be concentrations compared to boulder samples from ridge locations, when accounting for their protrusion height as a relative indicator for exposure time. An exception is again found in LC, at Cerro Cabra.

227   **4.2   Bedrock, boulder, and soil denudation rates**

228   Bedrock denudation rates in NA range from 8.53 ± 0.6 m Myr^{-1} to 18.64 ± 1.4 m Myr^{-1}, and

229   the LC bedrock sample yielded a denudation rate of 22.28 ± 2.62 m Myr^{-1}. We modelled boulder

230   (ϵ_s) and soil denudation rates (ϵ_s) using the approach described in section 3.1.3 for all boulder

231   samples that have higher concentrations than the adjacent soil concentrations. We address

232   locations where ^{10}Be concentrations are higher in soil compared to boulder samples in the

233   discussion (three locations in LC and one in NA). In contrast to the bedrock denudation rates,

234   modelled boulder and soil denudation rates have no unique solution, and their range of possible

235   denudation rates is more complex (Fig. 5). However, not every combination within the range

236   plotted in Fig. 5 is likely. For example, the part of the colored bands in Fig. 5 that is close to the

237   1:1-line (edge of the gray area) exists because at very low differential denudation rates

238   (differences between soil and boulder denudation rates), phase 2 gets very long so that the

239   boulder denudation rate dominates the resulting concentration and approaches the value one

240   would obtain when neglecting the first term on the right side in Eq. 1. We argue that differential

241   denudation rates of less than ~1 m Myr^{-1} are highly unlikely, as it would take ~1 Myr to exhume a

242   boulder of only 1 m in height above the soil, while simultaneously eroding many times more soil

243   and boulder material.

244   In NA, modelled soil denudation rates range from ~13 to 37 m Myr^{-1} and modelled

245   boulder denudation rates range from ~5 to 20 m Myr^{-1} (Fig. 5A). Three samples that were taken

246   from the same ridge at Cerro Anay (Fig. 2C and 4A) all overlap in denudation rate despite

247   varying protrusion heights. These samples also overlap with a sample from Casa de Piedras, and

248   together indicate a rather narrow range of soil and boulder denudation rates of ~15-20 m Myr^{-1}

249   and ~10-15 m Myr^{-1}, respectively. Only the mid-slope sample from Cerro Anay has higher

250   modelled soil and boulder denudation rates. In LC, modelled boulder and soil denudation rates

251 that are consistent with the measured ^{10}Be concentrations extend to much higher values compared

252 to the other field sites (40-140 m Myr^{-1}) and the two solutions do not overlap. In SG, modelled

253 denudation rates are similar in magnitude to results from NA (Fig. 5C); soil denudation rates

254 range from ~10 to 28 m Myr^{-1} and boulder denudation rates range from ~5 to 23 m Myr^{-1}.

255 Samples taken from the ridge of Santa Gracia Hill (Fig. 2I and 4C) have modelled soil and

256 boulder denudation rates that overlap at values of ~12-15 m Myr^{-1} and ~10-12 m Myr^{-1},

257 respectively. Samples from the slope of Santa Gracia Hill have higher modelled soil denudation

258 rates, when considering very low differential denudation rates unlikely.

259 **4.3   Fault and stream orientations**

260   Fault orientations in our field sites, based on straight segments of 100 m (8,731 segments

261 for SG, 6,572 segments for LC, and 6,214 segments for NA), generally have at least one

262 dominant orientation that aligns with stream orientations (Fig. 6). Stream orientations depend on

263 the flow accumulation threshold: at smaller thresholds (10^4 m^2), many small streams are selected,

264 giving a large distribution of orientations that reflects the shape of the catchment as a whole. At a

265 high flow accumulation threshold (10^6 m^2), the derived stream networks comprise only the largest

266 channels and their orientation is strongly controlled by the orientation and tilt of the drainage

267 basin. This can be seen clearly in NA, where the east-west oriented trunk stream is weighted

268 heavily. In SG, faults and stream orientations match each other well, both trending north-south. In

269 LC and NA, one of two regional fault orientations matches stream orientations, and faults closest

270 to the field sites more closely match dominant stream orientations (red faults in Fig. 6).

271 Specifically, in LC, the dominant orientations for the regional faults are roughly northeast and

272 secondarily northwest, whereas streams are generally oriented northwest. In NA, faults generally

273   have east-west and northwest-southeast orientations, and streams with an accumulation threshold

274   above 10^4 follow an east-west orientation.

275   **5   Discussion**

276   **5.1   Deciphering the true denudation rates of boulders and soil**

277   Our model results show that there exist no unique combination of soil and boulder

278   denudation rates for any particular site (Fig. 5). Which, then, are the most likely combinations of

279   boulder and soil denudation rates? The answer depends on the characteristic exhumation histories

280   of the boulders, and events that could have influenced the accumulation of ^{10}Be during the course

281   of exhumation. In order to narrow down the ranges of denudation rates for boulders and soils

282   investigated in this study, we address several complicating factors, such as shielding and toppling

283   of boulders, and compare measured and modelled ^{10}Be concentrations of soils to each other.

284   **5.1.1   Shielding and toppling of boulders**

285   When sampling, two ways to inadvertently introduce bias include: 1) sampling material

286   that remains in situ, but has been previously shielded by a boulder, or 2) sampling a boulder that

287   has toppled or rolled downhill, and is no longer in situ. In both cases, the actual production rate

288   for the sample could be lower than assumed, leading to an artificially high denudation rate

289   estimate. The first scenario is more likely in areas where there are tall, densely-clustered

290   boulders, or at protruding bedrock outcrops such as Piedra de Aguila, where we measured a very

291   low ^{10}Be concentration in sample NB-BR4 (Table 1; Fig. 4A). This sample was taken from a

292   bedrock knob close to a cliff in an area accessed by tourists; it is possible that the low

293   concentration of our sample is due to shielding by boulders or bedrock blocks that toppled from

294   the sampled area.

295   The second scenario is more likely in areas with steep slopes. In LC, where slopes are

296   generally steeper than the other field sites, it is possible that some boulders were not in situ when

297   we sampled them: they could have rolled or been overturned on the steep slopes, uncovering a

298   side that was previously shielded. Indeed, three boulder samples from LC (LC2, LC4, and LC18;

299   Table 1) have measured ^{10}Be concentrations that are lower than the surrounding soil, violating

300   our model assumptions, and suggesting that the boulders were shielded. Two of these samples

301   (LC4 and LC18) were collected from slopes with rather high angles of 27° and 18°, respectively,

302   and therefore could have toppled downslope, but LC2 was collected on a ridge with a relatively

303   lower slope of 9° (Table 1). For LC2, the low concentration could stem from shielding by stacked

304   boulders (scenario 1). In NA, one boulder sample (NA15; Table 1) also has a very low ^{10}Be

305   concentration and was not included in the model. We did not collect a soil sample near the

306   boulder sample NA15, and instead compared its concentration to the adjacent surficial soil pit

307   sample of Schaller et al. (2018). Because these samples were not taken exactly next to each other,

308   there exists some ambiguity in this comparison. However, the relatively low ^{10}Be concentrations

309   of sample NA15 when compared to other boulder samples in NA suggest issues that could be

310   related to shielding or toppling of boulders.

311   **5.1.2   Most likely ranges for modelled denudation rates**

312   Most of our soil samples have measured ^{10}Be concentrations that are similar to ^{10}Be

313   concentrations calculated using our modelled denudation rates (Table 2), supporting the

314   reliability of the model results. Positive or negative deviations are expected, however, because (1)

315   soil samples we collected in the field are most likely a mixture between lower concentrations in

316   soil that is directly exhumed from below, and higher concentration grains eroded from the

317   surrounding boulders, and (2) we did not account for shielding of soil by the surrounding

318   boulders, which would lower production rates. In one case (Casa de Piedras in NA), the measured

319   soil [10]Be concentration is significantly lower than the modelled soil [10]Be concentration (Table 2).

320   If the soil was eroding as fast as our measured soil samples indicate, the boulders should be

321   protruding higher. However, Casa de Piedras has a high density of tall boulders. The observed

322   discrepancy could be caused by boulders shielding the soil directly surrounding it from cosmic

323   rays, or by eroding chips with low [10]Be concentrations of shielded parts of the boulders, perhaps

324   from the base, that erode directly into the soil.

325   Next, we identify the most likely range of denudation rates for each sample type and

326   location for all modelled denudation rates. Specifically, we chose denudation rate ranges for

327   samples on Cerro Anay ridge and Casa de Piedras based on their overlap with each other, for

328   samples on Cerro Anay slope based on their overlap with sample NA9 on Cerro Anay ridge, and

329   ranges for Santa Gracia hill ridge and slope based on the overlap of modelled rates for each

330   respectively (Fig. 5). For LC we chose denudation rates near the center of the modelled curves in

331   Figure 5, based on realistic expectations of differential erosion (section 4.2), and considering

332   possible issues with shielding and toppling (section 5.1). These ranges are listed in Table 2 along

333   with measured and modelled [10]Be concentrations of soil samples, and are displayed in Fig. 7

334   along with previously published soil (Schaller et al., 2018) and catchment-average denudation

335   rates (van Dongen et al., 2019). In the following section, we discuss the erosional processes that

336   may account for the differences and similarities in denudation rates from bedrock, boulders, soil

337   (this study and Schaller et al., 2018), and stream sediment (van Dongen et al., 2019) within each

338   field site.

5.2 Processes controlling differential erosion

339

340   In NA, the slowest denudation rates occur on bedrock and boulders, likely because

341 precipitation runs off quickly, limiting chemical alteration (Eppes and Keanini, 2017) and

342 weathering (Hayes et al., 2020), whereas soils erode faster. However, denudation rates for soil

343 surrounding the sampled boulders are lower than denudation rates from the soil pit and the

344 catchment average denudation rates. It is possible that boulders physically block soil from being

345 transported downslope: where a dense clustering of exhumed boulders exists, the regolith will be

346 thinner, and the boulders likely retard soil erosion throughout the area in which they are clustered

347 (Glade et al, 2017). Where soil is thicker, if slopes are steep enough, shallow landsliding can

348 occur, as observed in NA by Terweh et al. (2021). In accordance with these observations, van

349 Dongen et al (2019) found that smaller grains in stream sediment were likely derived from the

350 upper mixed soil layer, and the largest grains were likely excavated from depth, perhaps by

351 shallow landsliding. The smaller grains have denudation rates similar to those presented in this

352 study (Fig. 7), while larger grains have denudation rates similar to deeper soil pit samples from

353 Schaller et al. (2018).

354   Finally, in NA, where bedrock fracture density is higher, denudation rates are also higher

355 (Fig. 7), likely because precipitation infiltrates into fractures, accelerating chemical weathering,

356 regolith formation (St. Claire et al., 2015; Lebedeva and Brantley, 2017), and subsequent

357 vegetation growth, which introduces biotic acids that further accelerate chemical weathering

358 (Amundson et al., 2007). We further speculate that large exhumed boulders in NA are also sites

359 of less-fractured bedrock at depth, as boulders can only be as large as the local fracture spacing

360 allows (e.g. Sklar et al., 2017). Based on the observed differences in soil, boulder, and fractured

361 bedrock denudation rates in NA, and on previous studies that have correlated higher fracture

362 density with more rapid erosion (e.g., Dühnforth et al., 2010; Dibiase, 2018; Neely et al., 2019),

363   we suggest that bedrock fractures have an effect on NA's morphology through grain size

364   reduction and differential erosion. Further, the thicker soil cover and shallow landsliding on NA

365   slopes may increase the discrepancy between slowly-eroding, less-fractured bedrock and boulders

366   versus more rapidly-eroding, vegetation-covered hillslopes, eventually causing bedrock and

367   boulders to sit at topographic highs, as we observed in the field.

368   In the semi-arid landscape of SG, as in humid-temperate NA, boulders are eroding more

369   slowly than the surrounding soil, but the differences in boulder and soil denudation rates are

370   subtle. In addition, denudation rate differences between ridge and slope samples – possibly

371   related to slope angle – are larger than the differences between boulders and soil. Furthermore,

372   unlike in NA, our boulder and soil denudation rates are similar to the soil pit and catchment

373   average denudation rates (Fig. 7), suggesting that erosional efficiencies are similar across

374   different sediment sizes. Uniform ^{10}Be concentrations across grain sizes is in accordance with

375   absent landsliding (Terweh et al., 2021). Van Dongen et al. (2019) also measured relatively

376   constant catchment average ^{10}Be concentrations over seven grain size classes in SG (Fig. 7),

377   which suggests that all grain sizes must have been transported from the upper mixed layer of

378   hillslope soil, and that deep-seated erosion processes are unlikely. Thus, our results agree with

379   previous findings that erosion in SG is likely limited to grain-by grain exfoliation of boulders and

380   the slow diffusive creep of the relatively thin soil cover on hillslopes (Schaller et al., 2018). When

381   bedrock is exhumed, its long residence time on hillslopes allows it to weather slowly in place and

382   reduce in size, with minimal transportation of weathered material by runoff and a low degree of

383   chemical weathering and soil production (Schaller and Ehlers, 2022).

384   Such a narrow range of relatively low denudation rates indicates that very long time

385   periods are necessary to produce relief between hilltops and valleys. Note, however, despite low

386   uplift rates in SG, the total mean basin slope in SG is 17° compared to 9° in NA (van Dongen et

387   al., 2019). This could be due to low MAP resulting in a low erosional efficiency in SG; in order

388   to achieve denudation rates that match uplift rates, slopes in arid climates must be steeper

389   (Carretier et al., 2018). Although the differences in denudation rates between grain sizes is subtle

390   in SG, soils have higher denudation rates than the boulders they directly surround, suggesting

391   that, if the boulders are delineated by fractures at depth as we infer for NA, fractures could also

392   have an effect on landscape morphology in SG. Additionally, Krone et al (2021) noted that the

393   fractures in a drill core in SG were rimmed by halos of weathered material depleted in soluble

394   elements, and concluded that the fractures act as pathways for fluid transport into the subsurface,

395   which enhances chemical weathering. In summary, we suggest that fractures likely accelerate

396   chemical weathering and erosion in SG, but the resultant differential denudation rates are subtle

397   due to low MAP and low tectonic uplift rates.

398   In LC we observe the largest range of denudation rates between bedrock, boulders, soil,

399   and stream sediment, and also the highest overall denudation rates of the three field sites. We

400   suspect that both of these characteristics are related to slope angles, which are on average nearly

401   twice as steep as in NA and SG (Table 1; van Dongen et al., 2019). It should be noted that the

402   stream sediment samples were taken from an adjacent catchment that does not drain the hillslopes

403   sampled in this study, and the generally low and wide-ranging [10]Be concentrations in the stream

404   sediment have been related to relatively recent landslides observed in the upper headwaters (van

405   Dongen et al., 2019; Terweh et al., 2021). However, steep slopes are pervasive throughout LC

406   and lead us to suggest that shallow landslides are important erosional processes in this field site

407   too.

408   In LC we frequently observed boulder samples with lower [10]Be concentrations than

409   adjacent soil samples (Table 1, section 5.1), which is inconsistent with our simple model of

410   boulder exhumation (Fig. 3), and is possibly because the sampled boulders were not exhumed in

411   situ (section 5.1.1). Landslides as observed in LC can bring down boulders in the processes of

412   downhill movement, and may cause the excavation of larger blocks from greater depth before

413   their size is reduced in the weathering zone. More vigorous mass wasting is consistent with larger

414   average hillslope grain sizes for LC, as compared to NA and SG (Terweh et al., 2021). In general,

415   the high relief, steep slopes, and high denudation rates in LC suggest that tectonic uplift rates

416   could be higher than assumed for the nearby coast (Melnick et al., 2016). Finally, although the

417   role that fracturing plays in LC is difficult to assess, note that our bedrock sample has a

418   significantly lower denudation rate than boulders and soils (Fig. 7), despite being on a steep slope

419   (Table 1). If we assume that the bedrock patch has a lower fracture density than the boulders

420   based on previous studies that correlate fracture spacing with grain size (e.g. Sklar et al., 2017;

421   Dibiase et al., 2018; Neely et al., 2019), then the slower denudation rate of the bedrock patch

422   could be an effect of fracture spacing in LC.

423   Overall, each field site presents a different pattern of denudation rates between bedrock,

424   boulders, soil, stream sediment, and soil pits. The patterns of differential erosion between the

425   field sites are likely dictated by a combination of tectonics (differences in uplift and fracture

426   spacing) and the local climate regime.

5.3   Fracture control on larger-scale landscape evolution

428   In NA, we were able to measure fracture density in several bedrock outcrops and found

429   that higher fracture density is correlated with higher denudation rates (Fig. 7), and we suggest that

430   patterns in fracture density affect the landscape morphology. We were not able to measure

431   fracture density in the other two field sites due to the scarcity of bedrock exposure. However, we

432   suspect that fractures may also play a role in their landscape morphology, and this may be visible

433   on a larger scale, through similarity of fault and stream orientations.

434   As tectonically-induced faults and fractures are products of the same regional stresses, we

435   assume that regional faults have orientations consistent with fractures in our field sites (c.f.,

436   Krone et al., 2021). We observe that stream channels in our field sites ($A_{min} \geq 10^5\,m^2$) generally

437   follow fault orientations (Fig. 6), presumably because faults and fractures reduce grain size and

438   allow easier transport of hillslope material and directing stream incision (Roy et al., 2016). This is

439   especially clear in SG, where the north-south striking Atacama Fault System is reflected in the

440   orientation of faults, streams, and also fractures measured in a nearby drill core (Krone et al.,

441   2021; Fig. 6). In LC and NA, despite more variety in fault and stream orientations, faults closest

442   to the field sites tend to align with stream orientations (Fig. 6). Especially in NA, the larger

443   streams are often nearly perpendicular to each other, similar to rectangular drainage networks,

444   which are often indicative of structural control on drainage patterns (e.g., Zernitz, 1932). We

445   speculate that over geologic time scales, smaller streams are more transient features, whereas the

446   larger ones are more persistent. These results suggest that within the same rock type, local

447   fracture patterns induced by regional faults can induce differential denudation in landscapes.

448   Further, such differential denudation rates have the ability to shift the landscape from steady

449   state. If faults are inclined, the location of fractured bedrock will shift over time as bedrock is

450   exhumed and erodes, thus also shifting the locations of streams, valleys, and topographic highs

451   over time, and introducing topographic disequilibrium to the landscape (Roy et al., 2016).

452   In summary, we argue that in NA, and likely also in SG and LC, bedrock fracturing

453   influences landscape morphology by setting grain size and thus dictating patterns of denudation

454   rates on hillslopes and in streams. We therefore offer the following conceptual model: in a

455   landscape with fractured bedrock (Fig. 8A), areas with higher fracture density should be sites of

456   smaller sediment sizes (e.g. Sklar et al., 2017; Neely and Dibiase, 2020), where rainfall can easily

457   infiltrate, conversion of bedrock to regolith is easiest (St. Claire et al., 2015; Lebedeva and

458   Brantley, 2017), and denudation rates are highest. Over time, precipitation will divergently run

459   off topographic highs and starve bedrock and boulders on high points while infiltrating into

460   topographic lows, where streams eventually incise (Bierman, 1994; Hayes et al., 2020; Fig. 8B).

461   Regolith also promotes vegetation growth, which slows runoff, raises rates of infiltration, and

462   enhances chemical weathering (Amundson et al., 2007), creating a positive feedback between

463   precipitation and fracture density (Fig. 8B). Additional fractures due to topographic stresses from

464   exhumation may also form at topographic highs as the topography emerges (St. Claire et al.,

465   2015), countering this positive feedback loop (Fig. 8C). Over longer timescales, bedrock with

466   different patterns of fracture density may be exhumed, which can invert landscapes to reflect the

467   new fracture patterns exposed at the surface (Roy et al., 2016). In this way, fracturing, climate,

468   and residence time can operate in conjunction to set the sediment size and morphology of

469   hillslopes and streams within landscapes.

470   **6   Conclusions**

471   In this study, we tested the ability of bedrock patches and large boulders to retard

472   denudation and influence landscape morphology, in relatively slowly-eroding landscapes along a

473   climate gradient in the Chilean Coastal Cordillera. Based on in-situ cosmogenic [10]Be-derived

474   denudation rates of bedrock, boulders and soil, we find that (1) in almost all cases across the three

475   sites studied, soil denudation rates are higher than the denudation rates of the boulders that they

476   surround; (2) hillslope denudation rates increase with fracture density in NA; and (3) streams tend

477   to follow the orientation of larger faults. These results suggest that large hillslope boulders affect

478   landscape morphology through differential denudation rates: soil erodes from around bedrock

479   patches and boulders, exposing these features over time. Eventually, the largest boulders and

480   bedrock patches in a landscape should become topographic highs due to their overall lower

481 denudation rates than soil; therefore, we predict that current bedrock patches on hillslopes are

482 nuclei for future peaks and ridges.

483   Our results also support the concept that bedrock patches and boulders represent locations

484 where fracture density is lower, and thus weathering, erosion, and soil formation are suppressed.

485 Precipitation runs off topographic highs where intact bedrock is exposed, and infiltrates into soils

486 on hillslopes and in valleys, promoting chemical weathering below. Bedrock fracture density

487 affects denudation rates by damaging bedrock, reducing grain size, and making it easier to be

488 removed by erosional processes. On a larger scale, our results imply that tectonic preconditioning

489 in the form of bedrock faulting and fracturing influences landscape evolution by impacting the

490 pathway of streams, as well as the migration of ridges, drainage divides and knickpoints, as

491 landscapes erode through layers of bedrock preconditioned by tectonic fracturing over time, and

492 encounter varying levels of resistance depending on the fracture density.

493

494 **7 Acknowledgements**

495   This work was supported by the German Science Foundation (DFG) priority research

496 program SPP-1803 "EarthShape: Earth Surface Shaping by Biota" (grant SCHE 1676/4-2 to D.

497 S.). We thank the Chilean National Park Service (CONAF) for providing access to the sample

498 locations and on-site support of our research. We also thank Iris Eder and David Scheer for their

499 help in the field and in the laboratory, and Steven A. Binnie and Stefan Heinze from Cologne

500 University for conducting AMS measurements.

501

502

503 **8 Data Availability**

504 Cosmogenic nuclide data presented in this paper will be made available as a GFZ Data

505 Publication in accordance with FAIR principles. LiDAR data from the studied catchments is

506 available at Krüger et al. (2022).

507 **9 References**

508 Amundson, R., Richter, D. D., Humphreys, G. S., Jobbágy, E. G., Gaillardet, J., 2007. Coupling

509 between biota and earth materials in the critical zone. Elements. 3 (5), 327-333.

510 10.2113/gselements.3.5.327.

511 [dataset] ASF DAAC 2021, ALOS PALSAR_Radiometric_Terrain_Corrected_high_res;

512 Includes Material © JAXA/METI 2009-2011. Accessed through ASF DAAC 3 December 2021.

513 https://doi.org/10.5067/Z97HFCNKR6VA.

514 Attal, M., Mudd, S. M., Hurst, M. D., Weinman, B., Yoo, K., Naylor, M, 2015. Impact of change

515 in erosion rate and landscape steepness on hillslope and fluvial sediments grain size in the Feather

516 River basin (Sierra Nevada, California). Earth Surf. Dynam. 3, 201–222.

517 https://doi.org/10.5194/esurf-3-201-2015.

518 Balco, G., Stone, J. O., Lifton, N. A., Dunai, T. J., 2008. A complete and easily accessible means

519 of calculating surface exposure ages or erosion rates from 10Be and 26Al measurements. Quat.

520 Geochronol. 3, 174–195. https://doi.org/10.1016/j.quageo.2007.12.001.

521 Bierman, P., 1994. Using in situ produced cosmogenic isotopes to estimate rates of Landscape

522 evolution: A review from the geomorphic perspective. J. Geophys. Res.: Solid Earth. 99 (B7),

523 13885-13896. https://doi.org/10.1029/94JB00459.

524 Boisier, J. P., Alvarez-Garretón, C., Cepeda, J., Osses, A., Vásquez, N., Rondanelli, R., 2018.

525 CR2MET: A high-resolution precipitation and temperature dataset for hydroclimatic research in

526 Chile. Geophys. Res. Abstr. 20(Vic), 2018–19739.

527 Borchers, B., Marrero, S., Balco, G., Caffee, M., Goehring, B., Lifton, N., Nishiizumi, K.,

528 Phillips, F., Schaefer, J., Stone, J., 2016. Geological calibration of spallation production rates in

529 the CRONUS-Earth project. Quat. Geochronol. 31, 188-198.

530 https://doi.org/10.1016/j.quageo.2015.01.009.

531 Braucher, R., Merchel, S., Borgomano, J., Bourlès, D.L., 2011. Production of cosmogenic

532 radionuclides at great depth: A multi element approach. Earth Planet. Sc. Lett. 309, (1–2), 1-9.

533 https://doi.org/10.1016/j.epsl.2011.06.036.

534 Burbank, D. W., Leland, J., Fielding, E., Anderson, R. S., Brozovic, N., Reid, M. R., and Duncan,

535 C., 1996. Bedrock incision, rock uplift and threshold hillslopes in the northwestern Himalayas.

536 Nature. 379, 505–510. https://doi.org/10.1038/379505a0.

537 Carretier, S., Tolorza, V., Regard, V., Aguilar, G., Bermúdez, M.A., Martinod, J., Guyot, J-L,

538 Hérail, G., Riquelme, R., 2018. Review of erosion dynamics along the major N-S climatic

539 gradient in Chile and perspectives. Geomorphology. 300, 45-68.

540 https://doi.org/10.1016/j.geomorph.2017.10.016.

541 Clair, J. St., Moon, S., Holbrook, W.S., Perron, J.T., Riebe, C.S., Martel, S.J., 2015. Geophysical

542 imaging reveals topographic stress control of bedrock weathering. Geomorphology. 350 (6260).

543 Coira, B., Davidson, J., Mpodozis, C., Ramos, V., 1982. Tectonic and Magmatic Evolution of the

544 Andes of Northern Argentina and Chile. Earth-Science Reviews. 18, 303-332.

545   Dewald, A., Heinze, S., Jolie, J., Zilges, A., Dunai, T., Rethemeyer, J., Melles, M., Staubwasser,

546   M., Kuczewski, B., Richter, J., Radtke, U., von Blanckenburg, F., Klein, M., 2013. Cologne

547   AMS, a dedicated center for accelerator mass spectrometry in Germany. Nucl. Instrum. Meth. B

548   294, 18-23. dx.doi.org/10.1016/j.nimb.2012.04.030

549   DiBiase, R. A., Rossi, M. W., Neely, A. B., 2018. Fracture density and grain size controls on the

550   relief structure of bedrock landscapes. Geology. 46 (5), 399–402.

551   https://doi.org/10.1130/G40006.1

552   Dietrich, W.E., Bellugi, D.G., Sklar, L.S., Stock, J.D., Heimsath, A.M., Roering, J.J., 2003.

553   Geomorphic transport laws for predicting landscape form and dynamics. Geophysical

554   Monograph-American Geophysical Union. 135, 103-132.

555   Dühnforth, M., Anderson, R.S., Ward, D., Stock, G.M., 2010. Bedrock fracture control of glacial

556   erosion processes and rates. Geology. 38 (5), 423-426. https://doi.org/10.1130/G30576.1.

557   Eppes, M. C., and Keanini, R., 2017. Mechanical weathering and rock erosion by climate-

558   dependent subcritical cracking. Review of Geophysics. 55 (2), 470-508.

559   Glade, R. C., Anderson, R. S., Tucker, G. E., 2017. Block-controlled hillslope form and

560   persistence of topography in rocky landscape. Geology. 45 (4), 311–314.

561   https://doi.org/10.1130/G38665.1

562   Glodny, J., Graaefe, K., Rosenau, M., 2008. Mesozoic to Quaternary continental margin

563   dynamics in South-Central Chile (36–42∘ S): the apatite and zircon fission track perspective. Int.

564   J. Earth Sci. 97, 1271–1291. https://doi.org/10.1007/s00531-007-0203-1.

565   Granger, D. E., Riebe, C. S., Kirchner, J. W., Finkel, R. C., 2001. Earth Planet. Sc. Lett. 186,

566   269-281.

567   Hayes, N. R., Buss, H. L., Moore, O. W., Krám, P., Pancost, R. D., 2020. Controls on granitic

568   weathering fronts in contrasting climates. Chemical Geology. 535, 119450.

569   https://doi.org/10.1016/j.chemgeo.2019.119450.

570   Kirby, E., Whipple, K.X., 2012. Expression of active tectonics in erosional landscapes. Journal of

571   Structural Geology. 44, 54-75. https://doi.org/10.1016/j.jsg.2012.07.009.

572   Krone, L.V., Hampl, F.J., Schwerdhelm, C., Bryce, C., Ganzert, L., Kitte, A., Übernickel, K.,

573   Dielforder, A., Aldaz, S., Oses-Pedraza, R. Perez, J.P.H., 2021. Deep weathering in the semi-arid

574   Coastal Cordillera, Chile. Scientific Reports. 11(1), 1-15.

575   Kügler, M., Hoffmann, T. O., Beer, A. R.; Übernickel, K.; Ehlers, T. A.; Scherler, D., Eichel, J.,

576   2022. (LiDAR) 3D Point Clouds and Topographic Data from the Chilean Coastal Cordillera. V.

577   1.0. GFZ Data Services. https://doi.org/10.5880/fidgeo.2022.002.

578   Lal, D., 1991. Cosmic ray labeling of erosion surfaces: in situ nuclide production rates and

579   erosion models. Earth Planet. Sc. Lett. 104, 424–439.

580   Lebedeva, M. I., Brantley, S. L., 2017. Weathering and erosion of fractured bedrock systems.

581   Earth Surf. Proc. Land. 42, 2090–2108. https://doi.org/10.1002/esp.4177.

582   Melnick, D., 2016. Rise of the central Andean coast by earthquakes straddling the Moho, Nat.

583   Geosci. 9, 1–8. https://doi.org/10.1038/ngeo2683.

584   Molnar, P., Anderson, R.S., Anderson, S.P., 2007. Tectonics, fracturing of rock, and erosion, J.

585   Geophys. Res. 112, F03014. https://doi.org/10.1029/2005JF000433.

586   Neely, A.B., DiBiase, R.A., Corbett, L.B., Bierman, P.R., Caffee, M.W., 2019. Bedrock fracture

587   density controls on hillslope erodibility in steep, rocky landscapes with patchy soil cover,

588   southern California, USA. Earth Planet. Sc. Lett. 522, 186-197.

589   https://doi.org/10.1016/j.epsl.2019.06.011.

590   Neely, A.B., DiBiase, R.A., 2020. Drainage Area, Bedrock Fracture Spacing, and Weathering

591   Controls on Landscape-Scale Patterns in Surface Sediment Grain Size. J. Geophys. Res. Earth

592   Surf. 125, (10). https://doi.org/10.1029/2020JF005560.

593   Oberlander, T. M., 1972. Morphogenesis of Granitic Boulder Slopes in the Mojave Desert,

594   California, J. Geol., 80, 1–20.

595   Oeser, R. A., Stroncik, N., Moskwa, L., Bernhard, N., Schaller, M., Canessa, R., Brink, L. Van

596   Den, Köster, M., Brucker, E., Stock, S., Pablo, J., Godoy, R., Javier, F., Oses, R., Osses, P.,

597   Paulino, L., Seguel, O., Bader, M. Y., Boy, J., Dippold, M. A., Ehlers, T. A., Kühn, P.,

598   Kuzyakov, Y., Leinweber, P., Scholten, T., Spielvogel, S., Spohn, M., Übernickel, K., Tielbörger,

599   K., Wagner, D., and Blanckenburg, F. Von, 2018. Chemistry and microbiology of the Critical

600   Zone along a steep climate and vegetation gradient in the Chilean Coastal Cordillera. Catena.

601   170, 183–203. https://doi.org/10.1016/j.catena.2018.06.002.

602   Perron, J.T., 2011. Numerical methods for nonlinear hillslope transport laws. J. Geophys. Res.

603   Earth Surf. 116 (F2). https://doi.org/10.1029/2010JF001801.

604   Portenga, E.W., Bierman, P.R., 2011. Understanding earth's eroding surface with 10Be. GSA

605   Today. 21, 4–10. https://doi.org/10.1130/G111A.1.

606   Roda-Boluda, D.C., D'Arcy, M., McDonald, J., Whittaker, A.C., 2018. Lithological controls on

607   hillslope sediment supply: insights from landslide activity and grain size distributions. Earth Surf.

608   Proc. Land. 43, 956–977. https://doi.org/10.1002/esp.4281.

609   Roy, S. G., Tucker, G. E., Koons, P. O., Smith, S. M., Upton, P., 2016. A fault runs through it:

610   Modeling the influence of rock strength and grain-size distribution in a fault-damaged landscape.

611   J. Geophys. Res. Earth Surf. 121, https://doi.org/10.1002/2015JF003662.

612   Schaller, M., Ehlers, T.A., Lang, K.A.H., Schmid, M., and Fuentes-Espoz, J.P., 2018. Addressing

613   the contribution of climate and vegetation cover on hillslope denudation, Chilean Coastal

614   Cordillera (26◦–38◦S). Earth Planet. Sc. Lett. 489, 111–122.

615   https://doi.org/10.1016/j.epsl.2018.02.026.

616   Schaller, M., Ehlers, T.A., 2022. Comparison of soil production, chemical weathering, and

617   physical erosion rates along a climate and ecological gradient (Chile) to global observations.

618   Earth Surface Dynamics. 10 (1), 131-150. https://doi.org/10.5194/esurf-10-131-2022.

619   Schwanghart, W., Scherler, D., 2014. Short Communication: Topo Toolbox 2 – MATLAB-based

620   software for topographic analysis and modeling in Earth surface sciences. Earth Surf. Dynam. 2,

621   1–7. https://doi.org/10.5194/esurf-2-1-2014.

622   [dataset] SERNAGEOMIN, 2003. Mapa Geológico de Chile: versión digital. Servicio Nacional

623   de Geología y Minería, Publicación Geológica Digital. No. 4 (CD-ROM, versión1.0). Santiago.

624   Shobe, C. M., Tucker, G. E., Anderson, R. S., 2016. Hillslope-derived blocks retard river

625   incision. Geophys. Res. Lett. 43, 5070–5078. https://doi.org/10.1002/2016GL069262.

626   Sklar, L. S., Riebe, C. S., Marshall, J. A., Genetti, J., Leclere, S., Lukens, C. L., Merces, V.,

627   2017. The problem of predicting the size distribution of sediment supplied by hillslopes to rivers.

628   Geomorphology. 277, 31–49. https://doi.org/10.1016/j.geomorph.2016.05.005.

629   Small, E.E., Anderson, R.S., Repka, J.L., Finkel, R.St., 1997. Erosion rates of alpine bedrock

630   summit surfaces deduced from in situ 10Be and 26A1. Earth Planet. Sc. Lett. 150, 413-425.

631   Stone, J.O., 2000. Air pressure and cosmogenic isotope production. Journal of Geophysical

632   Research: Solid Earth 105, no. B10, 23753-23759.

633   Terweh, S., Hassan, M.A., Mao, L., Schrott, L., Hoffmann, T.O., 2021. Bio-climate affects

634   hillslope and fluvial sediment grain size along the Chilean Coastal Cordillera. Geomorphology.

635   384, 107700. https://doi.org/10.1016/j.geomorph.2021.107700.

636   van Dongen, R., Scherler, D., Wittmann, H., von Blanckenburg, F., 2021. Cosmogenic 10Be in

637   river sediment: where grain size matters and why. Earth Surf. Dynam. 7, 393–410,

638   https://doi.org/10.5194/esurf-7-393-2019.

639   van Dongen, 2021. Discharge variability and river incision along a climate gradient in central

640   Chile. PhD thesis. Potsdam, Germany.

641   von Blanckenburg, F., Hewawasam, T., Kubik, P.W., 2004. Cosmogenic nuclide evidence for

642   low weathering and denudation in the wet, tropical highlands of Sri Lanka. J. Geophys. Res. 109,

643   F03008. https://doi.org/10.1029/2003JF000049.

644   Zernitz, E.R., 1932. Drainage patterns and their significance. The Journal of Geology. 40 (6),

645   498-521. https://doi.org/10.1086/623976.

646

647

648

649

650

651

652

10   Tables

654
655   Table 1. ^{10}Be cosmogenic nuclide sample data.

656
657

Sample ID	IGSN [a]	Sampling location[b]	Latitude (°N)	Longitude (°E)	Sample type [c]	^{10}Be conc. ±1σ (×10^5) (atoms g^{-1})	^{10}Be conc. normalized by SLHL ±1σ (×10^5) (atoms g^{-1})[d]	^{10}Be production rate (spallation, atoms g^{-1} yr^{-1})	Site scaling factor [e]	Slope angle at sample location (°) [f]	Avg. boulder width / protrusion or fracture density [g]	No. chips taken for sample
						Nahuelbuta						
NB-BR1	GFRD1002U	PdA ridge 1	-37.826	-73.035	BR	8.25±0.28	2.92±0.10	11.41	2.82	18	7.83	20
NB-BR2	GFRD1002V	PdA ridge 2	-37.821	-73.034	BR	6.92±0.24	2.43±0.09	11.44	2.85	4	4.75	15
NB-BR3	GFRD1002W	PdA ridge 3	-37.819	-73.032	BR	5.18±0.20	1.86±0.07	11.15	2.78	3	2	15
NB-BR4	GFRD10029	PdA ridge 4	-37.825	-73.034	BR	3.85±0.14	1.36±0.05	11.46	2.84	16	4.78	15
NA3	GFEL10002	PdA slope	-37.826	-73.034	BR	6.55±0.23	2.38±0.08	11.25	2.75	25	4.43	30
NA4	GFEL10003	CdP	-37.817	-73.031	B	9.08±0.32	3.49±0.12	10.43	2.60	5	1.70 / 0.68	30
NA7	GFEL10006	CA ridge	-37.789	-72.998	B	10.28±0.36	3.65±0.13	11.3	2.81	10	1.52 / 1.00	10
NA8	GFEL10007	CA ridge	-37.789	-72.998	B	8.94±0.31	3.18±0.11	11.3	2.81	10	3.30 / 2.43	10
NA9	GFEL10008	CA ridge	-37.789	-72.998	B	7.57±0.27	2.69±0.09	11.3	2.81	10	0.64 / 0.19	10
NA11	GFEL1000A	CA slope	-37.790	-72.999	B	7.67±0.26	2.76±0.09	11.18	2.78	14	1.90 / 1.60	10
NA15	GFEL1000E	SPH slope	-37.807	-73.013	B	2.84±0.069	1.12±0.03	10.24	2.53	18	0.96 / 0.76	12
NA5	GFEL10004	CdP	-37.817	-73.031	S	2.32±0.10	0.89±0.04	10.43	2.60	5	N/A	N/A
NA10	GFEL10009	CA ridge	-37.789	-72.998	S	5.04±0.18	1.79±0.06	11.3	2.81	10	N/A	N/A
NA12	GFEL1000B	CA slope	-37.790	-72.999	S	4.27±0.16	1.54±0.06	11.18	2.78	14	N/A	N/A
						La Campana						
LC-BR2	GFRD1002X	CC slope	-32.938	-71.081	BR	1.83±0.11	1.38±0.08	5.75	1.33	39	N/A	15
LC2	GFEL1002J	CC ridge	-32.939	-71.081	B	0.92±0.089	0.59±0.06	6.25	1.55	9	0.95 / 0.54	10
LC4	GFEL1003V	CC slope	-32.938	-71.079	B	0.92±0.083	0.66±0.06	5.77	1.40	27	0.30 / 0.15	10
LC11	GFEL1000Q	CG ridge	-32.941	-71.074	B	1.21±0.070	0.76±0.04	6.42	1.59	13	1.32 / 0.70	10
LC13	GFEL1000S	CG upper slope	-32.94	-71.073	B	0.73±0.080	0.51±0.06	6.13	1.43	33	0.32 / 0.20	12
LC18	GFEL1000Z	CG lower slope	-32.937	-71.074	B	1.55±0.079	1.17±0.06	5.43	1.32	18	0.50 / 0.32	12
LC1	GFEL1002H	CC ridge	-32.939	-71.081	S	1.54±0.092	0.99±0.06	6.25	1.55	9	N/A	N/A
LC3	GFEL1003W	CC slope	-32.938	-71.079	S	1.03±0.086	0.74±0.06	5.77	1.40	27	N/A	N/A
LC12	GFEL1000R	CG ridge	-32.941	-71.074	S	0.88±0.044	0.55±0.03	6.42	1.59	13	N/A	N/A
LC14	GFEL1000T	CG upper slope	-32.94	-71.073	S	0.63±0.037	0.44±0.03	6.13	1.43	33	N/A	N/A
LC19	GFEL1000X	CG lower slope	-32.937	-71.074	S	1.84±0.071	1.39±0.05	5.43	1.32	18	N/A	N/A
						Santa Grácia						
SG8	GFEL10017	SGH ridge	-29.756	-71.166	B	5.94±0.21	4.17±0.15	5.72	1.42	10	1.10 / 0.80	10
SG9	GFEL10018	SGH ridge	-29.756	-71.166	B	4.7±0.17	3.30±0.12	5.72	1.42	10	0.38 / 0.12	10
SG11	GFEL1001A	SGH slope 1	-29.758	-71.166	B	3.56±0.13	2.61±0.10	5.56	1.36	21	1.30 / 0.87	9
SG22	GFEL1001M	SGH slope 2	-29.758	-71.166	B	3.85±0.15	2.83±0.11	5.56	1.36	22	0.37 / 0.24	11
SG10	GFEL10019	SGH ridge	-29.756	-71.166	S	2.58±0.11	1.81±0.08	5.72	1.42	10	N/A	N/A
SG12	GFEL1001B	SGH slope 1	-29.758	-71.166	S	2.39±0.089	1.75±0.07	5.56	1.36	21	N/A	N/A
SG23	GFEL1001N	SGH slope 2	-29.758	-71.166	S	2.1±0.083	1.54±0.06	5.56	1.36	22	N/A	N/A

[a]Open access metadata: http://igsn.org/[insert IGSN number here]
[b]Sample locations: SGH: Santa Gracia Hill, CC: Cerro Cabra, CG: Cerro Guanaco, PdA: Piedra de Aguila, CdP: Casa de Piedas, CA: Cerro Anay, SPH: Soil Pit Hill.
[c]Sample type abbreviations: BR: bedrock, B: boulders, S: soil.
[d]Concentrations were normalized to SLHL (sea level high latitude) using a SLHL production rate of 4.01 atoms g-1 yr^{-1} (Borchers et al., 2016) and the site's scaling factor.
[e]Time constant spallation production rate scaling scheme of Lal (1991) and Stone (2000) ('St' in Balco et al., 2008).
[f]Local hillslope angles were calculated using a 12.5m DEM and an 8-connected neighbourhood method.
[g]Fracture density for bedrock (in meters) and width and protrusion measurements (in meters) for boulders. Values are averages of >10 measurements per sample site.

658

Table 2. Modelled denudation rates for soil and boulder samples using the first term of Eq. 1, and
comparison of modelled and measured [10]Be concentrations for soil samples. Sample location
abbreviations are described in the caption for Table 1.

662

Sample location	Soil sample ID	Best-fitting modelled soil denudation range rate (ϵ_s) (m Myr[-1])	Corresp. modelled range of [10]Be conc. (×10^{5}) (atoms g[-1]) for soil (N_m)	Measured [10]Be conc. ±1σ (×10^{5}) (atoms g[-1])	Boulder sample IDs	Best-fitting modelled boulder denudation rate range (ϵ_b) (m Myr[-1])
Nahuelbuta						
CdP	NA5	15-20	3.61-4.75	2.32±0.10	NA4	10-15
CA ridge	NA10	15-20	3.89-5.12	5.04±0.18	NA7, NA8, NA9	10-15
CA slope	NA12	18-20	3.84-4.25	4.27±0.16	NA11	15-18
La Campana						
CG ridge	LC12	70-90	0.54-0.69	0.88±0.04	LC11	40-60
CG upper slope	LC14	120-140	0.32-0.37	0.63±0.04	LC13	80-120
Santa Gracia						
SGH ridge	SG10	12-15	2.77-3.41	2.58±0.11	SG8, SG9	10-20
SGH slope 1	SG12	19-21	1.94-2.13	2.39±0.09	SG11	18-20
SGH slope 2	SG23	19-21	1.94-2.13	2.1±0.08	SG22	18-20

663
664
665
666

667 **11 Figures**
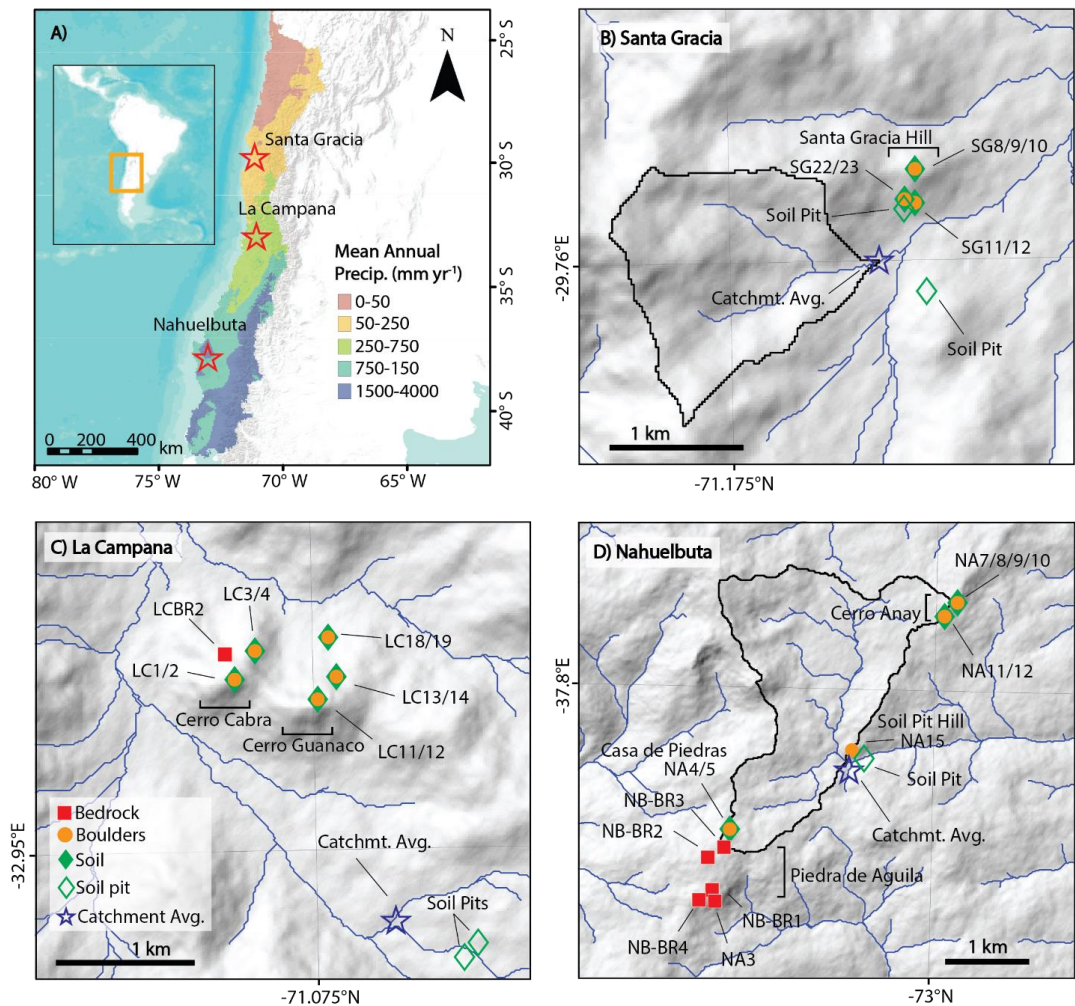
669   Figure 1. Field site locations and features. A) Map of mean annual precipitation in central Chile,
670   with field sites marked by red stars. Precipitation data from the CR2MET dataset, by the Center
671   for Climate and Resilience Research (CR^2) (Boisier et al., 2018), provides an average for the time
672   period 1979-2019. World Terrain Base map sources are Esri, USGS, NOAA. B-D: Hillshade
673   images from 12.5-m ALOS PALSAR digital elevation models, of B) Santa Gracia (SG), C) La
674   Campana (LC), and D) Nahuelbuta (NA). Sample locations and sample names are shown, with
675   symbol shape and color indicating the sample type (see legend in lower left panel). Black outlines
676   delineate the catchments from which the catchment average sample (star) was taken (the
677   catchment from La Campana does not fit within the bounds of the map and therefore is not
678   shown). Blue lines indicate streams. Soil pit sample data are from Schaller et al. (2018), and
679   catchment average sample data are from van Dongen et al. (2019).
680
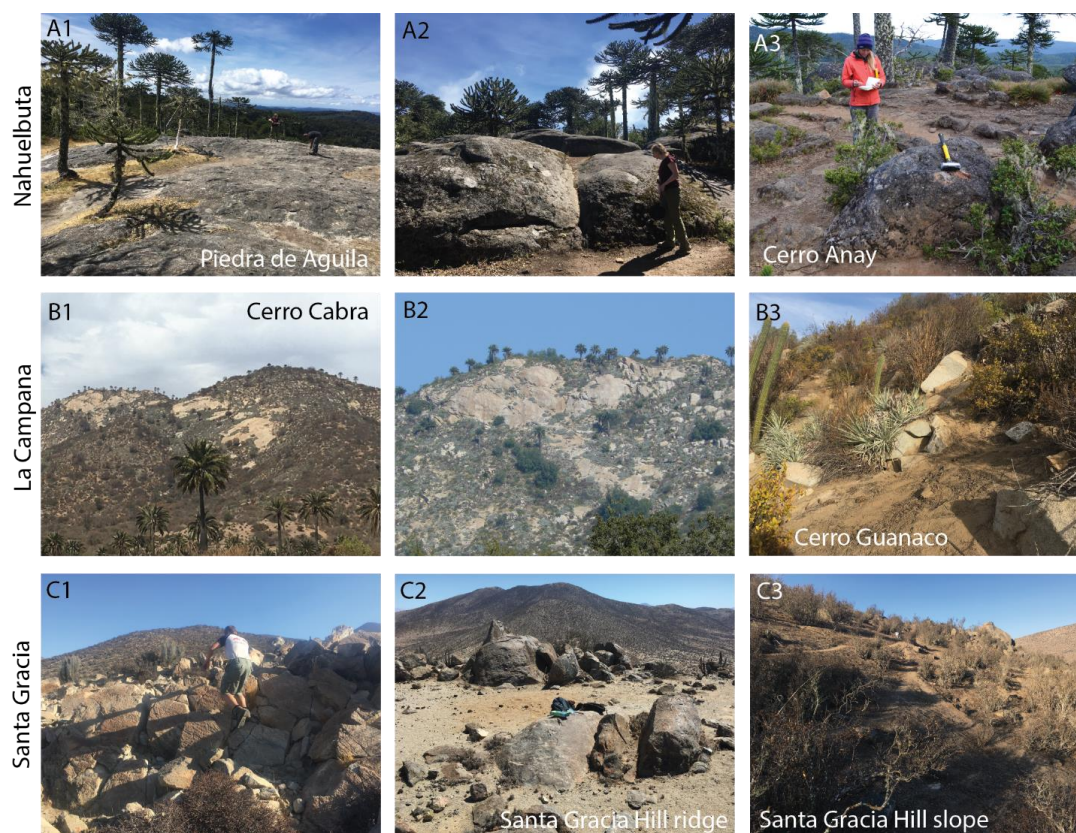
Figure 2. Field photos showing the various surfaces sampled, including bedrock, boulders and soil. A: Nahuelbuta, A1) Bedrock (sample NB-BR1). A2) Fractured bedrock, in transition between unfractured bedrock and boulders (sample NB-BR2). A3) Smaller boulders surrounded by soil (sample NA7). B: La Campana, B1) Bedrock (sample LC-BR2). B2) Bedrock transitioning to large boulders and soil. B3) Boulders and soil on a hillside (samples LC13 and LC14). C: Santa Gracia, C1) Boulders on a hillside delineated by fractures. C2) Large boulders on the ridge of Santa Gracia Hill (sample SG8). C3) Soil with minimal boulders on the slope of Santa Gracia Hill (samples SG22 and SG23).
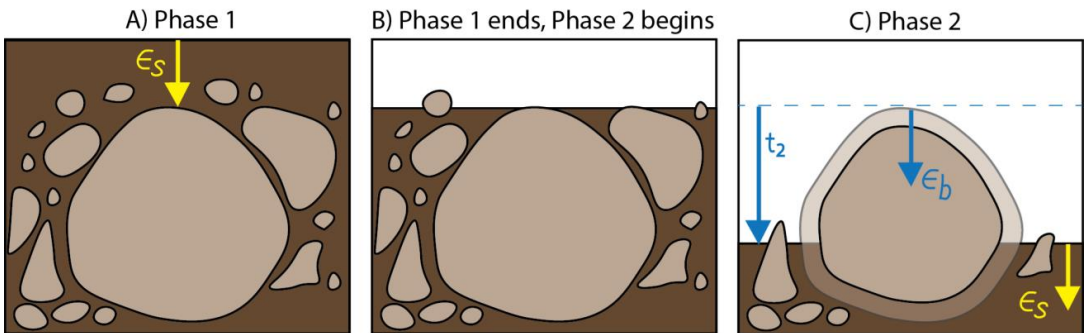
Figure 3. Schematic image showing the process of boulder exhumation. A) During phase 1, the boulder is buried, and accumulates nuclides at a rate governed by the soil denudation rate, ϵ_s. B) Phase 1 ends when the boulder breaches the soil surface. C) During phase 2, the boulder itself is eroding at a rate of ϵ_b, and the surrounding soil continues to erode at a rate of ϵ_s. Phase 2 lasts for a time period t_2 that ends with our sampling.
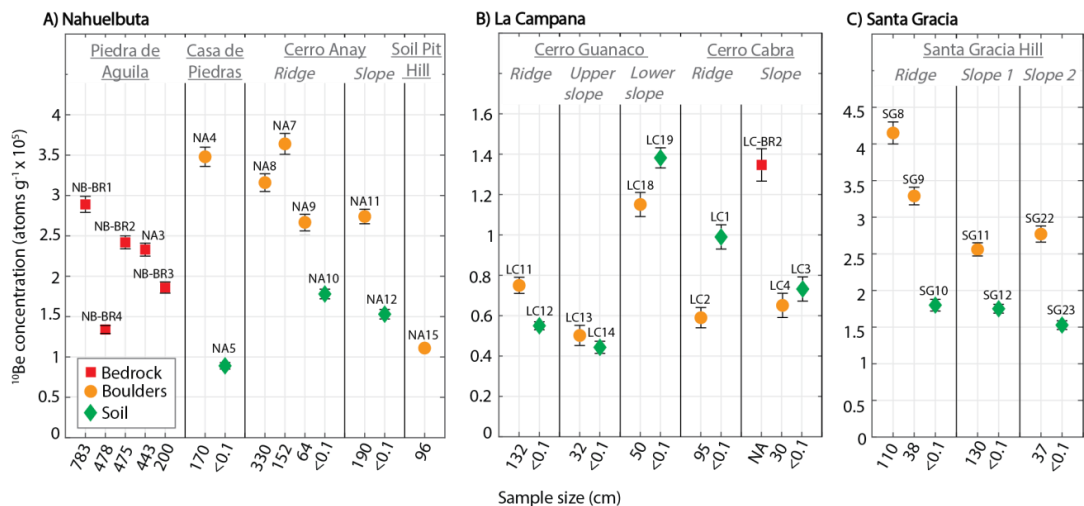
Figure 4. Measured ^{10}Be concentrations normalized to reference production rate at sea-level high latitude. A) Nahuelbuta, B) La Campana, and C) Santa Gracia; note different scales of y-axes. X-axes show the sample size (cm) of bedrock, boulder and soil samples. For bedrock samples, the sample size indicates the fracture density at the sample site. For boulder samples, the sample size indicates the average width (b-axis) of boulders from which we collected chips for an amalgamated sample. Soils are labeled <0.1 cm. Labels next to data points provide sample IDs, also reported in Table 1.

711
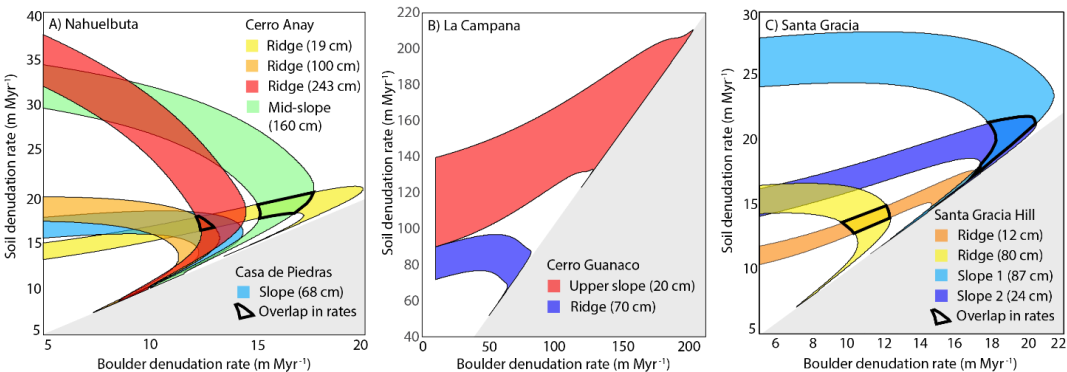
Figure 5. Range of best fitting combinations of modelled soil and boulder denudation rates in A)
Nahuelbuta, B) La Campana, and C) Santa Gracia according to Eq. 1. Each color band
corresponds to an amalgamated boulder sample, listed in the legend along with the average
protrusion height of the boulders. Areas where best fitting denudation rates overlap for samples
from the same location are highlighted by a black outline. The gray areas are forbidden fields, as
by assumption, boulder denudation rates have to be lower than soil denudation rates, otherwise
there would be no boulder protruding above the soil surface.

721
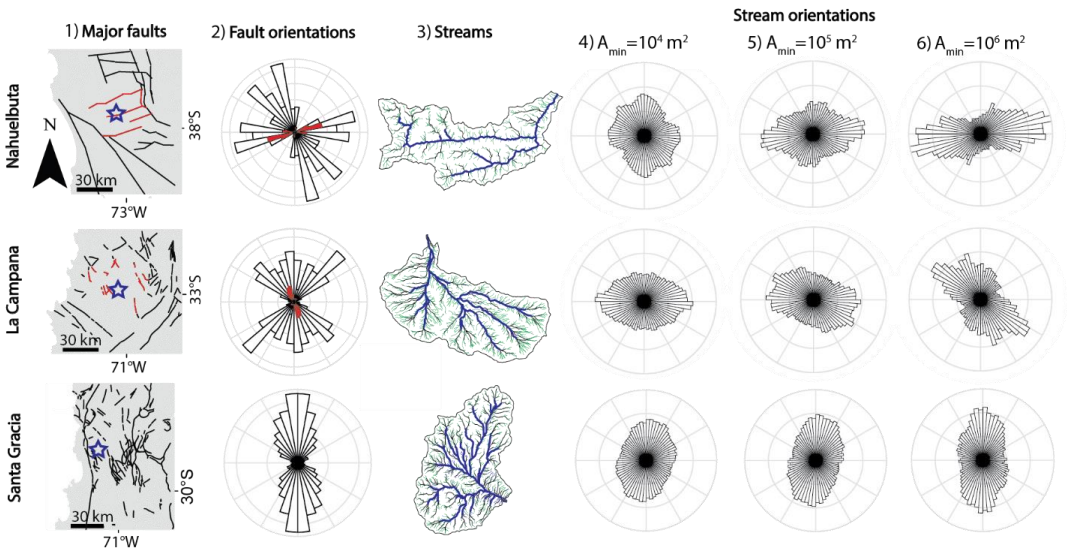
Figure 6. Rose diagram plots and maps showing fault and stream orientations for Nahuelbuta (top
row), La Campana (middle row), and Santa Gracia (bottom row). For each field site, the columns
show from left to right: (1) major faults digitized from geological map (SERNAGEOMIN, 2003),
within ~50 km (black) and ~25 km (red, NA and LC only) of the sampling site (blue star); (2)
rose diagram of fault orientations from the maps in column 1, constructed using 100 m long,
straight fault segments and 36 bins, with orientations of faults <25 km from NA and LC in red;

729 (3) a map of the studied catchments and the drainage network, with green, black, and blue
730 streams indicating minimum upstream areas (A_{min}) of 10^4, 10^5, and 10^6 m^2, respectively, derived
731 from one-meter resolution LiDAR DEMs (Kügler et al., 2022).; (4-6) rose diagrams (72 bins) of
732 stream orientations for different A_{min}. All maps and rose diagrams are oriented with the top being
733 north.

734
735
736

737
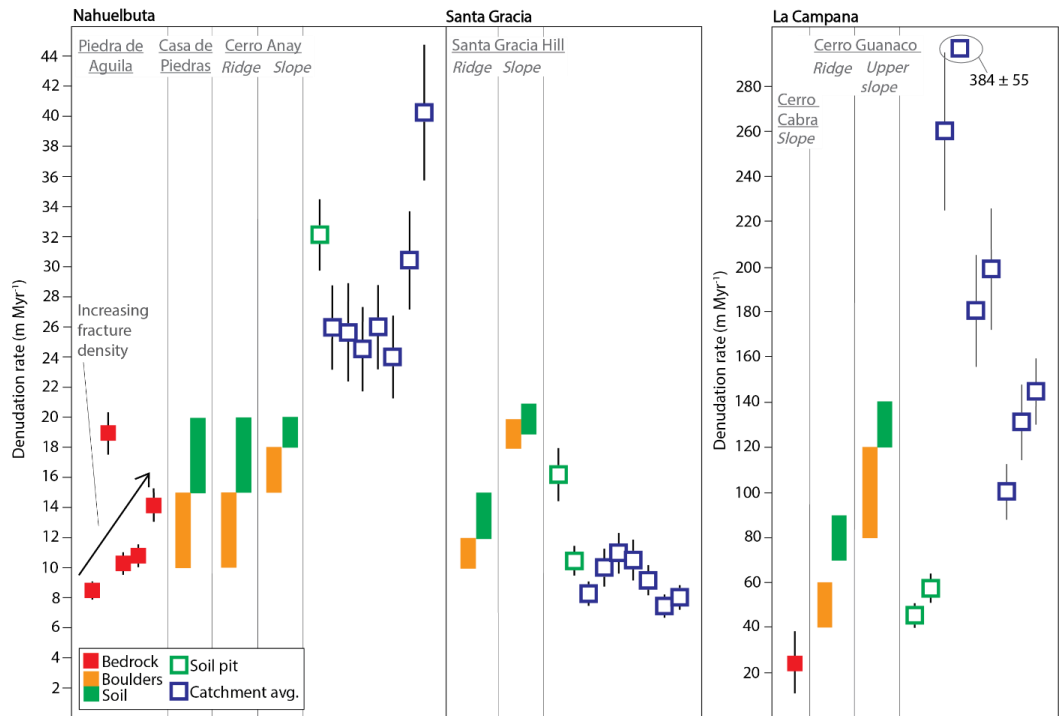
738 Figure 7. Overview of new and previously published denudation rates. Soil pit data from Schaller
739 et al. (2018), and catchment average data from van Dongen et al. (2019). Catchment average
740 denudation rates from various sediment grain sizes (from left to right for each field site: 0.5-1, 1-
741 2, 2-4, 4-8, 8-16, 16-32, and 32-64 mm). Bedrock denudation rates are calculated using the
742 CRONUS online calculator v2.3 (Balco et al., 2008). Boulder and soil denudation rates are
743 estimated using our model and reflect the most likely denudation rates as described in section
744 5.1.2. Denudation rates for each location within a field site are separated by thin gray bars, and
745 locations are labeled at the top of the chart. Samples that were not included in the model (one
746 sample from Nahuelbuta and 3 samples from La Campana) are also not included here. Data from
747 this study is shown by solid symbols and previously-published data is shown by hollow symbols.

748
749
750
751

752
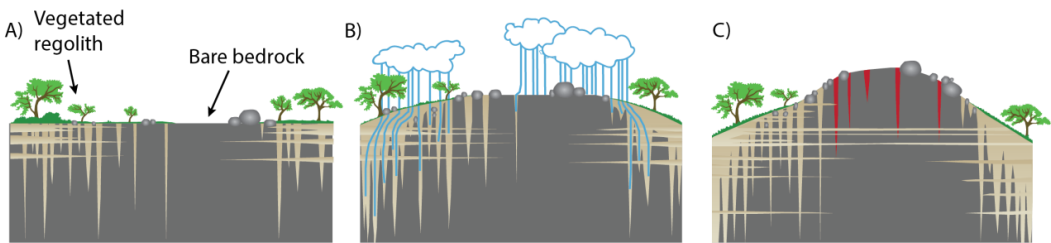
Figure 8: Schematic illustration showing influence of bedrock fractures on landscape evolution.
(A) Bedrock with different fracture densities is to different degrees infiltrated by rain and ground
water, which leads to differences in chemical weathering, soil formation and vegetation growth,
resulting in different hillslope sediment sizes. (B) Differential denudation between highly
fractured and less fractured areas induce relief growth, which further promotes spatial gradients
in chemical weathering, hillslope sediment size, and denudation. (C) Growing relief increases
topographic stresses and formation of new fractures (red) at topographically high positions (e.g.,
St. Clair et al., 2015).